CHEMISTRY OF MATERIALS

pubs.acs.org/cm

Article

Role of Adsorbate Coverage on the Oxygen Dissociation Rate on Sr-Doped $LaMnO_3$ Surfaces in the Presence of H_2O and CO_2

Jing Yang,[‖] Jonathan M. Polfus,*[,‖] Zuoan Li, Harry L. Tuller, and Bilge Yildiz*

Cite This: *Chem. Mater.* 2020, 32, 5483−5492

Read Online

ACCESS | Metrics & More | Article Recommendations | Supporting Information

ABSTRACT: Sr-doped $LaMnO_3$ (LSM) is a promising oxygen reduction reaction electrocatalyst in solid oxide fuel cells and other electrochemical devices. The presence of CO_2 and H_2O has been reported to promote the oxygen dissociation reaction on LSM surfaces. Here, we investigate the coadsorption mechanism of O_2 with H_2O or CO_2 by combining first-principles calculations of the (0 0 1) surface containing 25−100% Sr with thermodynamic adsorption models. The molecules were found to chemisorb by formation of charged oxygen, hydroxide, and carbonate species, and the adsorption energies were exothermic up to monolayer coverage. Low concentrations of H_2O or CO_2 do not compete with O_2 for adsorption sites under relevant conditions. However, their presence contributes to the total amount of oxygen-containing species. The increased coverage of oxygen species provides a quantitative explanation for the reported enhancement in oxygen dissociation kinetics in the presence of H_2O/CO_2. This study thereby provides insights into oxygen exchange mechanisms on LSM surfaces.

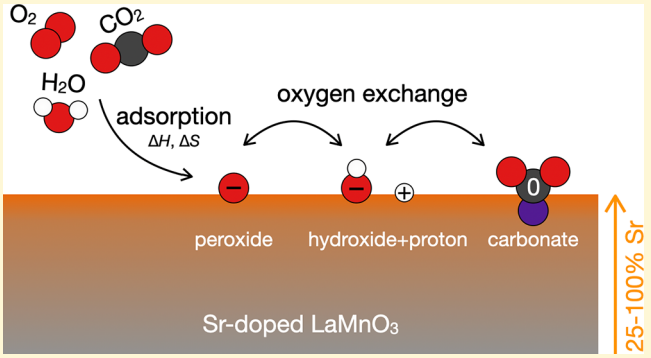

1. INTRODUCTION

Sr-doped $LaMnO_3$ (LSM) is one of the most studied perovskite materials for solid oxide fuel cell (SOFC) cathodes because of its high electronic conductivity, good oxygen reduction kinetics, and thermal and chemical stability with yttria-stabilized zirconia.[1−3] For the same reasons, LSM has also been applied in composite electrodes in solid oxide electrolyser cells[4] and catalytic layers and/or electronically conducting phases for mixed conducting membranes and catalytic membrane reactors.[5] At intermediate temperatures (600−800 °C), the main limiting factor for the performance of SOFCs has been ascribed to the oxygen reduction reaction (ORR) at the cathode.[3,6] Oxygen surface exchange and surface diffusion of oxide ions have been identified as two key processes that control the ORR.[7] Surface exchange kinetics remains an elusive property because it involves several steps including adsorption and dissociation of molecular oxygen, reduction (charge transfer), and incorporation of oxygen species into the cathode or electrolyte. Depending on the specific application and electrode characteristics, there are multiple possible reaction pathways, and it is inherently challenging to separate individual reaction steps.[8,9]

LSM has been found to catalyze oxygen exchange mainly through the homoexchange mechanism where LSM provides surface sites for the adsorbates to dissociate, diffuse, and reassociate.[10] Oxygen is subsequently incorporated into the electrolyte at the triple-phase boundaries, which may be the limiting step of the ORR.[11] On the other hand, the heteroexchange mechanism involves lattice oxygen and thereby requires oxygen vacancies at the surface. Although LSM exhibits low bulk oxygen vacancy concentration, heteroexchange may be facilitated by fast diffusion along grain boundaries.[12,13] In the case of typical mixed conducting cathode materials such as $La_2NiO_{4+\delta}$ and $Ba_{0.5}Sr_{0.5}Co_{0.8}Fe_{0.2}O_{3-\delta}$, dissociative adsorption of oxygen—rather than incorporation—has been reported to limit the oxygen surface exchange.[14,15]

In situ isotope-labeled gas-phase exchange experiments have been used to investigate the oxygen exchange reaction. By flowing gas mixtures of $^{18}O_2$ and $^{16}O_2$ over a catalyst bed, the oxygen dissociation rate can be measured directly as the steady-state concentration of the dissociation product, $^{18}O^{16}O$. In such experiments, the oxygen exchange rate can be directly related to the oxygen adsorbate concentration in the case of the homoexchange mechanism. With this approach, Huang et al. recently showed that the presence of H_2O and CO_2 could enhance the oxygen dissociation rate on LSM surfaces.[16] By adding 2500−3000 ppm of CO_2 or H_2O to pure 0.05 bar

Received: December 18, 2019
Revised: June 4, 2020
Published: June 5, 2020

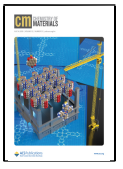

oxygen, the oxygen dissociation rate increased by a factor of 1.5−2 and the results showed that both CO_2 and H_2O participated in the exchange reaction. The detailed understanding of this improvement is still unclear; possible explanations could be the presence of additional oxygen-containing surface species such as hydroxide or carbonate or changes in the reaction mechanisms and/or barriers as suggested for $La_{0.6}Sr_{0.4}Co_{0.2}O_{3-\delta}$[17] and $SrTiO_3$.[18]

In the case of other materials systems, few studies have been performed on the effect of steam on oxygen surface exchange: isotope exchange followed by SIMS measurements has revealed enhanced oxygen surface exchange for mixed conductors such as $La_{0.6}Sr_{0.4}FeO_{3-\delta}$[19] and $PrBaCo_2O_{5+\delta}$[20] in the presence of steam, which was ascribed to faster water adsorption and dissociation at surface oxygen vacancies, that is, heteroexchange. On the other hand, the presence of CO_2 impurities usually has an adverse effect on oxygen surface exchange kinetics because of undesirable reactions and/or degraded performance of the cell.[21,22]

In this work, we predict the equilibrium adsorbate concentrations on LSM surfaces by combining first-principles calculations and thermodynamic models for gas adsorption. The (La, Sr)O-terminated (0 0 1) surface is selected as the model system as it is shown to be the favored termination in theoretical and experimental studies.[23,24] We consider the cases of O_2/CO_2 and O_2/H_2O coadsorption as a function of partial pressures and temperature. The role of coadsorption can thereby be evaluated in comparison with measured oxygen dissociation rates under given environmental conditions.[16]

The surface adsorption reactions were described by considering chemisorption and dissociative adsorption. Adsorption of CO_2 by formation of a carbonate species can be described by bonding with an LSM surface oxide ion

$$CO_2(g) + {}^*O^{2-} = CO_{3,ad}{}^{2-} \quad (1)$$

where *O denotes a surface O-site. Chemisorption of carbonate species has been reported for $LaMnO_3$ and similar perovskites such as $SrTiO_3$, $BaZrO_3$, and $K_{1-y}Na_yTa_{1-x}Nb_xO_3$.[25−28] Second, the dissociative adsorption of water can be described according to

$$H_2O(g) + {}^*La/Sr = OH_{ad}{}^- + H_{ad}{}^+ \quad (2)$$

where *La/Sr denotes a surface La or Sr-site and $H_{ad}{}^+$ is associated with a surface oxide ion, that is, $OH_O^\bullet$ in Kröger−Vink notation.[29] Third, the dissociative adsorption of oxygen can be described by the formation of peroxide species or oxide ion adsorbates on La/Sr sites

$$\frac{1}{2}O_2(g) + {}^*O = O_{ad}{}^- \quad (3)$$

$$\frac{1}{2}O_2(g) + {}^*La/Sr = O_{ad}{}^{2-} \quad (4)$$

For O_2/H_2O coadsorption, the proton may associate with $O_{ad}{}^{2-}$ to form $2OH_{ad}{}^-$ (resulting in a different site occupancy than the combination of eqs 2 and 4)

$$H_2O(g) + O_{ad}{}^{2-} + {}^*La/Sr = 2OH_{ad}{}^- \quad (5)$$

By also considering the coverage dependence of the adsorption energetics, the temperature and pressure ranges, where the surface becomes saturated and coadsorption becomes competitive, can be evaluated. Thereby, we present a quantitative comparison of the changes in overall oxygen coverages and the enhancement in the oxygen dissociation rate by addition of H_2O and CO_2 reported by Huang et al.[16]

2. COMPUTATIONAL METHODS

2.1. First-Principles Calculations. Spin-polarized density functional theory (DFT) calculations were carried out using VASP[30] and the projector-augmented wave method.[31] PBE-generalized gradient approximation (GGA)[32] was used with the DFT + U approach by Dudarev et al.[33] and the on-site Coulomb interaction parameter for Mn was set to 4.0 eV based on previous studies.[34−37] The energy cutoff for the planewave basis set was 400 eV. The included valence electrons were La $5s^2p^6d^16s^2$, Sr $4s^25p^66s^2$, Mn $3p^6d^54s^2$, and O $2s^2p^4$.

The surface of Sr-doped $LaMnO_3$ was modelled as a symmetric (La, Sr)O-terminated (0 0 1) slab with a thickness of 11 atomic layers and 2 × 2 cell expansion in the lateral directions (108 atoms). The periodic images of the slab were separated by a vacuum region of about 25 Å. The calculations were performed with a 4 × 4 × 1 k-point grid, and the atomic positions were optimized until the residual forces were within 0.03 eV $Å^{-1}$. In order to avoid spurious structural distortion upon gas adsorption, the orthorhombic structure was used, and the lateral lattice parameters 7.78 and 7.99 Å were obtained from a 2 × 2 × 2 cell with a Sr-dopant concentration of 12.5%. The octahedral tilting in the slab was $a^+b^-c^-$ in Glazer notation.

By use of symmetric slabs, the surface dipole between the terminating $(LaO)^+$ and $(MnO_2)^-$ layers in stoichiometric (0 0 1) slabs was avoided.[23] The excess positive charge of the additional $4(LaO)^+$ layer in the 2 × 2 slab was compensated by four Sr-dopants. Slabs terminated with three different Sr concentrations were considered: $4(La_{0.75}Sr_{0.25}O)^{0.75+}$, $4(La_{0.5}Sr_{0.5}O)^{0.5+}$, and $4(SrO)^0$, that is, 25, 50, and 100% Sr, respectively. The tendency for segregation of Sr to the surface of LSM was thereby taken into account.[36] In the case of the slab with 25% Sr on the surface, the remaining two Sr-dopants were introduced in the subsurface layer to obtain a charge neutral cell. The overall Sr concentration was thereby 16.7% for the slabs terminated with 25−50% Sr and 33.3% for the fully SrO-terminated slab.

Because of the inherent challenge of representing the high-temperature paramagnetic state of LSM, ferromagnetic (half-metallic) ordering was imposed,[38] and the magnetic moment of Mn was 3.8−4.0 μ_b. Selected calculations were pursued with G-type antiferromagnetic ordering as it has been suggested as more appropriate to represent paramagnetic systems.[38] Although the antiferromagnetic ordering could not be retained upon adsorption, it has previously been shown not to be important for adsorption calculations in $LaMnO_3$.[39]

The adsorption energies, ΔE_i^{ads}, were calculated as the total energy difference of the adsorption reactions for coverages of 0.25, 0.5, and 1 monolayer. The adsorbates were generally introduced on both sides of the slab, while for some configurations, complete convergence was only achieved with the adsorbate on one side of the slab. The difference in adsorption energy for these two approaches was relatively small (typically ±0.1−0.17 eV). For calculations with higher coverages, the adsorbates were arranged in several symmetrically inequivalent configurations in order to obtain the lowest energy structure. Interactions between different adsorbates were investigated in the case of H_2O and O_2 according to reaction 5 (Supporting Information), but otherwise not considered. The calculated coverages may therefore be overestimated close to saturation, while the relative coverages of the different adsorbates can be expected to be less affected.

The adsorption thermodynamics were evaluated based on the adsorption energy and configurational and vibrational entropy of the adsorbates. The vibrational frequencies were obtained according to the finite displacement method implemented in VASP with four 0.015 Å displacements of the vibrating species along the crystallographic axes. The vibrational entropy of the adsorbates, S_i^{vib}, was thereby calculated from the normal mode frequencies, ν_j, according to

https://dx.doi.org/10.1021/acs.chemmater.9b05243
Chem. Mater. 2020, 32, 5483−5492

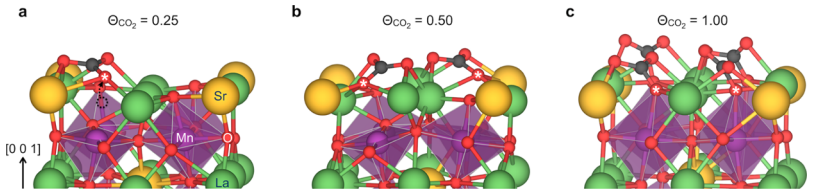

Figure 1. Chemisorbed CO_2 on LSM (0 0 1) with 25% Sr in the surface layer at coverages of a quarter monolayer (a), half monolayer (b), and full monolayer (c). The highlighted oxide ions originate from the LSM surface.

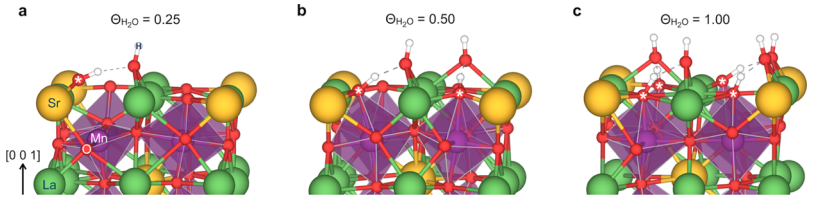

Figure 2. Dissociatively adsorbed H_2O on LSM (0 0 1) with 25% Sr in the surface layer at coverages of a quarter monolayer (a), half monolayer (b), and full monolayer (c). The highlighted oxide ions originate from the LSM surface.

$$S_i^{\mathrm{vib}} = -k\sum_j \left(\frac{\beta_j}{\exp(\beta_j) - 1} - \ln(1 - \exp(-\beta_j)) \right) \tag{6}$$

where $\beta_j = h\nu_j/kT$.[40] Changes in the vibrational frequencies of the LSM surface oxide ion were also included in the cases of $1/2O_2$ (peroxide), CO_2, H_2O adsorption. The change in zero-point energy upon adsorption, ΔZPE, was calculated using the same frequencies according to $\Delta\sum_j(h\nu j/2)$. The adsorption entropies, $\Delta S_i^{\mathrm{ads}}$, were obtained with the gaseous reference states taken from thermochemical tables[41] and therefore include the loss of translational entropy upon adsorption. Because of the challenges with the O_2 molecule within GGA, the chemical potential of O_2 was corrected based on the approach by Wang et al.[42] by normalizing the calculated enthalpies of formation of a range of binary nontransition metal oxides to the experimental values. The correction amounted to −1.14 eV for the total energy of the O_2 molecule (Figure S1).

2.2. Thermodynamic Model. The thermodynamic model computes equilibrium coverage for each adsorbate species by minimizing the total free energy of the system. Here, we list the energetic terms included in the model. For each adsorption species i, the total adsorption Gibbs energy associated with it is a function of its coverage Θ_i.

$$G_i^{\mathrm{ads}} = \Theta_i(\Delta H_i^{\mathrm{ads}} - T\Delta S_i^{\mathrm{ads}} - \Delta\mu_i) \tag{7}$$

Here, $\Delta H_i^{\mathrm{ads}} = \Delta E_i^{\mathrm{ads}}(\Theta_i) + \Delta\mathrm{ZPE}$ is the adsorption enthalpy for oxygen adatoms, water molecules, and carbon dioxide molecules as obtained from DFT calculations and $\Delta\mu_i = kT\ln(p/p^0)$ is the change in chemical potential of the gas species with varying partial pressure. The configurational entropy is given by the coverages of all adsorbates and is separated into contributions from the adsorbates associated with the oxygen and cation sites on the surface. The surface oxygen sites can be occupied by O_{ad}^-, H_{ad}^+, and carbon in $CO_{3,ad}^{2-}$, while the cation sites can be occupied by OH_{ad}^-, O_{ad}^{2-}, and oxygen in $CO_{3,ad}^{2-}$. Although each cation site can accommodate only one OH_{ad}^- or O_{ad}^{2-}, both oxygen atoms of $CO_{3,ad}^{2-}$ can be accommodated because of the specific adsorbate configuration upon carbonate formation. That is to say, each adsorbed CO_2 molecule occupies one oxygen site and one cation site on the surface. The total configurational entropy can thereby be written as

$$\begin{aligned} S_{\mathrm{config}} = -k[&\Theta_{CO_{3,ad}^{2-}}\ln\Theta_{CO_{3,ad}^{2-}} + \Theta_{H_{ad}^+}\ln\Theta_{H_{ad}^+} + \Theta_{OH_{ad}^-}\ln\Theta_{OH_{ad}^-} + \Theta_{O_{ad}^{2-}}\ln\Theta_{O_{ad}^{2-}} + \Theta_{O_{ad}^-}\ln\Theta_{O_{ad}^-} \\ &+ (1 - \Theta_{CO_{3,ad}^{2-}} - \Theta_{H_{ad}^+} - \Theta_{OH_{ad}^-}) \\ &\ln(1 - \Theta_{CO_{3,ad}^{2-}} - \Theta_{H_{ad}^+} - \Theta_{OH_{ad}^-}) \\ &+ (1 - \Theta_{O_{ad}^-} - \Theta_{O_{ad}^{2-}} - \Theta_{CO_{3,ad}^{2-}}) \\ &\ln(1 - \Theta_{O_{ad}^-} - \Theta_{O_{ad}^{2-}} - \Theta_{CO_{3,ad}^{2-}})] \end{aligned} \tag{8}$$

where either O_{ad}^{2-} or $\Theta_{O_{ad}^-}$ was included.

The total Gibbs energy of the system can thereby be described as

$$G_{\mathrm{tot}} = \sum_i G_i^{\mathrm{ads}} - TS_{\mathrm{config}} \tag{9}$$

where the sum over i covers all possible adsorbate species. The equilibrium coverages under given conditions were solved by varying the coverages of the coadsorbates and determining the combination of the lowest energy.

For the convenience of further analysis, we also define three additional coverage terms. First, the number of vacant cation adsorption sites, Θ_{free}, because these are limiting, allows for analyzing whether the surface is saturated by competitive adsorption

$$\Theta_{\mathrm{free}} = 1 - \Theta_O - \Theta_{H_2O} - \Theta_{CO_2} \tag{10}$$

Second, the total number of adsorbed oxygen species on the surface, $\Theta_{O_{tot}}$

$$\Theta_{O_{tot}} = \Theta_O + \Theta_{H_2O} + 2\Theta_{CO_2} \tag{11}$$

Third, the total number of adsorbed species on the surface, that is, counting only one of the oxygen atoms of CO_2

$$\Theta_{O+H_2O+CO_2} = \Theta_O + \Theta_{H_2O} + \Theta_{CO_2} \tag{12}$$

3. RESULTS

3.1. Adsorbate Configurations and Energies. Adsorption of CO_2 on LSM (0 0 1) was determined to be energetically most favorable by chemisorption of carbonate species as shown in Figure 1 for coverages of 0.25−1. The carbonate adsorbates were formed by bonding to an LSM surface oxide ion. For coverages of 0.25 and 0.5, the surface oxide ion(s) relaxed out of the LSM surface, leaving

https://dx.doi.org/10.1021/acs.chemmater.9b05243
Chem. Mater. 2020, 32, 5483−5492

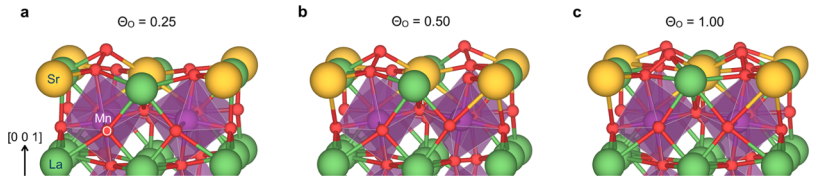

Figure 3. Chemisorbed oxygen as peroxide species on LSM (0 0 1) with 50% Sr in the surface layer at coverages of a quarter monolayer (a), half monolayer (b), and full monolayer (c).

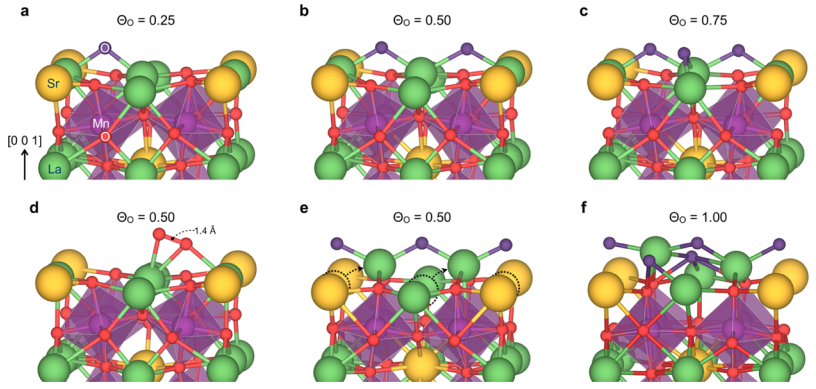

Figure 4. LSM (0 0 1) with 25% Sr in the surface layer and oxygen chemisorbed as bridging oxide ions: 0.25−0.75 monolayer (a−c), restructured surfaces with a half monolayer (e) and full monolayer (f), and a chemisorbed oxygen molecule (d).

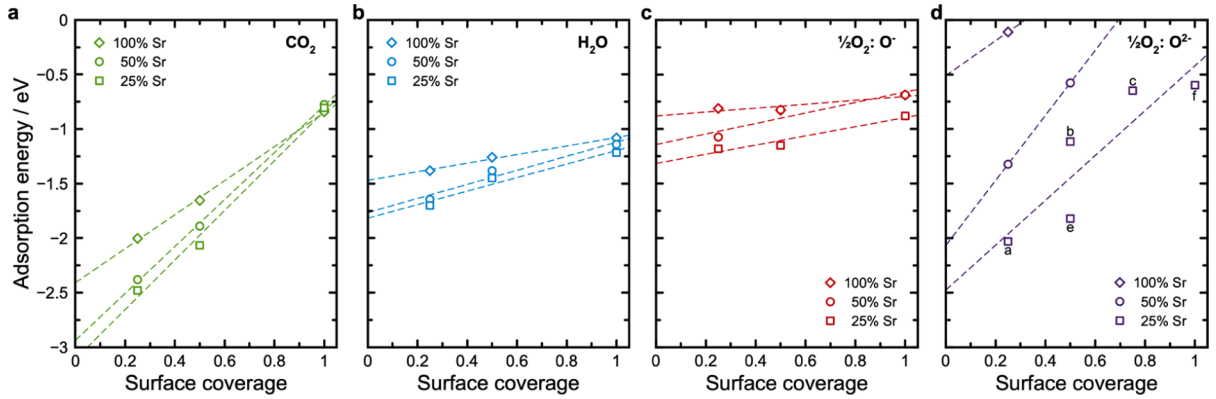

Figure 5. Coverage-dependent adsorption energies for chemisorbed CO_2 (a), H_2O (b), and oxygen as O^- (c) and various bridging configurations of O^{2-} according to Figure 4 (d).

undercoordinated manganese in the subsurface layer (Figure 1a,b).

The most stable configuration for dissociative adsorption of H_2O was determined to involve a hydroxide species bridging two surface cations, preferably La^{3+}, and a proton associated with a LSM surface oxide ion and directed toward the hydroxide species (Figure 2). Similar configurations of chemisorbed H_2O have been observed by scanning tunneling microscopy studies of the SrO-terminated surface of the layered perovskite $Sr_3Ru_2O_7$.[43] In some cases (Θ < 0.5, 25−50% Sr), the surface oxide ion relaxed out of the surface, leaving undercoordinated Mn in a similar manner as for the carbonate adsorbates.

Figure 3 shows oxygen chemisorbed as peroxide species bound to LSM surface oxide ions (reaction 3). The O−O bond lengths were 1.46−1.50 Å, that is, slightly longer than the nominal 1.4 Å, which may be ascribed to the additional bonding to the surface cations. Figure 4a−c shows chemisorption of oxygen by forming oxide ions bridging two surface cations (reaction 4) for coverages up to 0.75 monolayer. In the case of full coverage, some oxide ion adsorbates relaxed to peroxide species by associating with LSM surface oxide ions. For some configurations with coverages of 0.5 and higher, restructuring of the surface was observed by outward relaxation and displacement of La^{3+}, lowering the coordination to Mn at the surface from four to two (Figure 4e,f). Figure 4d shows the adsorption of an oxygen molecule with a bond length of 1.4 Å. In principle, the (0 0 1) surface contains four additional symmetrically equivalent sites for oxygen bridging Sr−La, but higher coverages resulted in significant restructuring of the surface and thus not considered further.

Bader charge analysis revealed that the bridging oxide ions attained essentially the same charge as the bulk oxide ions of LSM, $O^{-1.25}$. In comparison, the charge of oxygen in the dioxide configurations was significantly smaller: $O^{-0.7}$ for the dimer groups in Figure 3 and $O^{-0.5}$ for the O_2 molecule in Figure 4d, indicating that these species can be described as peroxide (O_2^{2-}) and superoxide (O_2^-), respectively.

https://dx.doi.org/10.1021/acs.chemmater.9b05243
Chem. Mater. 2020, 32, 5483−5492

Table 1. Adsorption Energies and Entropies for Chemisorption of CO_2, H_2O, and $1/2O_2$ on LSM (0 0 1) with 25−100% Sr in the Surface Layer and Site Occupancies for the Adsorbates[a]

gas		CO_2	H_2O	$1/2O_2$	
adsorbate		CO_3^{2-}	$OH^- + H^+$	O^-	O^{2-}
ΔE_{ads}/eV	25% Sr	$-3.11 + 2.27\Theta_{CO_2}$	$-1.82 + 0.62\Theta_{H_2O}$	$-1.32 + 0.42\Theta_O$	$-2.48 + 2.06\Theta_O$
	50% Sr	$-2.94 + 2.15\Theta_{CO_2}$	$-1.77 + 0.65\Theta_{H_2O}$	$-1.14 + 0.48\Theta_O$	$-2.07 + 2.98\Theta_O$
	100% Sr	$-2.41 + 1.56\Theta_{CO_2}$	$-1.47 + 0.39\Theta_{H_2O}$	$-0.88 + 0.18\Theta_O$	$-0.51 + 1.60\Theta_O$
ΔZPE/eV		0.068	0.061	0.032	0.015
ΔS_{ads}/eV K^{-1}		-1.70×10^{-3}	-1.60×10^{-3}	-9.27×10^{-4}	-9.15×10^{-4}
		$+1.5 \times 10^{-7}T$	$+2.3 \times 10^{-7}T$	$+9.2 \times 10^{-8}T$	$+1.1 \times 10^{-7}T$
adsorption site		La/Sr + O	La/Sr + O	O	La/Sr

[a]The oxygen adsorbates include peroxide (O^-) and configurations with bridging oxide ions (O^{2-}).

The calculated adsorption energies for LSM with 25, 50, and 100% Sr in the surface layer are shown as a function of adsorbate coverage in Figure 5 with corresponding linear fits. The adsorption energies were slightly less exothermic with increasing Sr content for all adsorbates, particularly at the lowest coverages. The adsorption energy of CO_2 showed the strongest coverage dependence, which may be ascribed to its larger size and the number of bonds to La/Sr, that is, steric and chemical interactions, respectively. In comparison, the H_2O and O^- adsorbates showed lower interactions both in terms of adsorption energies and structural relaxation. The adsorption energy of the O_2 molecule in Figure 4d was −2.82 eV (−1.41 eV per O), that is, in between the values for O^- and O^{2-} at comparable coverages of 0.25−0.5 (Figure 4a,b). The adsorption energies of bridging oxide ions exhibited a complex behavior and a strong dependence on both Sr content and adsorbate coverage. The most exothermic values ($\Theta \leq 0.5$, 25−50% Sr) may to a larger extent reflect the instability of the polar surfaces, as also evidenced by restructuring in some cases (e.g., Figure 4e). Notably, reverse segregation of Sr could be substantiated by considering the segregation energy for Sr combined with the adsorption energy of a bridging oxide ion. A segregation energy of −0.43 eV per Sr from the subsurface to surface was obtained by comparing the slabs with 25 and 50% Sr in the surface layer, while the adsorption energy of O^{2-} was −0.71 eV, more exothermic for the surface with 25% Sr. Accordingly, the most stable configuration was obtained with lower Sr content in the surface layer by including oxygen adsorbates. However, defects and mixed terminations must be considered for the complete understanding of the surface chemistry of LSM.[44,45]

Table 1 summarizes the thermodynamic parameters for adsorption and the respective site occupancies for the adsorbates. The vibrational frequencies of the adsorbates are provided in Table S1, and the temperature dependence and linear fit of the adsorption entropies are shown in Figure S2. Overall, the obtained adsorption energies are significantly exothermic for all three gases. In the case of CO_2, less exothermic chemisorption energies of −1.4 and −1.1 eV were previously obtained for the undoped material based on DFT calculations (using GGA and a different carbonate adsorption geometry) and adsorption isotherms on $LaMnO_{3.15}$ powders, respectively.[25] The present values for the Sr-doped surfaces range from −2.41 to −0.74 eV ($\Theta_{CO_2} = 0.25$). These values may be compared to the formation enthalpies of $La_2O_2CO_3$ and $SrCO_3$ from CO_2 and the binary oxides, −1.5[46] and −2.4 eV, respectively.[47] Similar CO_2 chemisorption energies have been reported for the BaO-terminated $BaZrO_3$ (−2.0 to −2.2 eV).[27,48] The obtained adsorption energies for dissociative adsorption of H_2O were in the same range as that reported for $LaMnO_3$ (−1.64 eV)[49] and other A-site terminated (layered) perovskites: $SrTiO_3$ (−1.1 eV),[50] $SrZrO_3$ (−1.5 eV),[51] $BaZrO_3$ (−1.4 to −1.5 eV),[52,53] and $Sr_3Ru_2O_7$ (−1.3 eV).[43] The oxygen adsorption energies correspond well with the value obtained by Piskunov et al. for the 25% Sr-doped (0 0 1) surface, −1.0 eV for $O^{-0.83}$ and −2.5 eV for $O^{-1.35}$ (Θ_O = 0.25).[54] It should be noted that several computational studies have been performed for oxygen adsorption on the MnO_2-terminated $LaMnO_3$ (0 0 1) surface.[34,37,55,56] The strong exothermic adsorption of both H_2O and CO_2 implies that these may enter competitive regimes. Consequently, the presence of H_2O may displace CO_2 and prevent carbonate formation on the surface as reported for $SrTiO_3$ and $BaZrO_3$.[18,53]

For the calculations of equilibrium adsorbate coverages, the peroxide configuration was considered because of the favorable energetics at higher coverages and across Sr contents compared to the bridging oxide ions. The restructuring observed for some of the bridging configurations may reflect permanent changes in the surface that alter the catalytic properties. Moreover, it remains uncertain if the most exothermic adsorption energies for the bridging configuration were associated with other aspects of the computational approach related to charge balance and surface polarity.

3.2. Adsorbate Coverages. The equilibrium adsorbate coverages were sought by minimizing the total Gibbs energy of the system as described in Section 2.2. To show how each energetic term changes with adsorbate coverages, Figure 6 displays the two-dimensional energy landscapes for CO_2/O^- coadsorption at T = 1073 K, $p_{O_2} = p_{CO_2}$ = 1 bar, and 50% Sr-doped surface. Figure 6a shows the total adsorption enthalpy $H_{ads} = \Theta_O \Delta H_O^{ads} + \Theta_{CO_2} \Delta H_{CO_2}^{ads}$. As ΔH_i^{ads} for both species is exothermic, the minimum H_{ads} is achieved on the line of $\Theta_O + \Theta_{CO_2} = 1$, with CO_2 slightly more favored. The entropic term $-TS_{ads}$ goes against surface saturation and contributes a large penalty to the total Gibbs energy with increasing coverages, as shown in Figure 6b. The configurational entropy, $-TS_{config}$, is minimized at intermediate total coverage, as both low coverage and saturation are low-entropy states (Figure 6c). The total Gibbs energy of the system is the sum of the previous three terms, with the first two being the dominant terms. In this case, the lowest energy is obtained for Θ_O = 0.31 and Θ_{CO_2} = 0.29. A similar plot for O_2/H_2O coadsorption is shown in Figure S4.

Following this method, the equilibrium surface coverages were surveyed for temperature and oxygen partial pressure

https://dx.doi.org/10.1021/acs.chemmater.9b05243
Chem. Mater. 2020, 32, 5483−5492

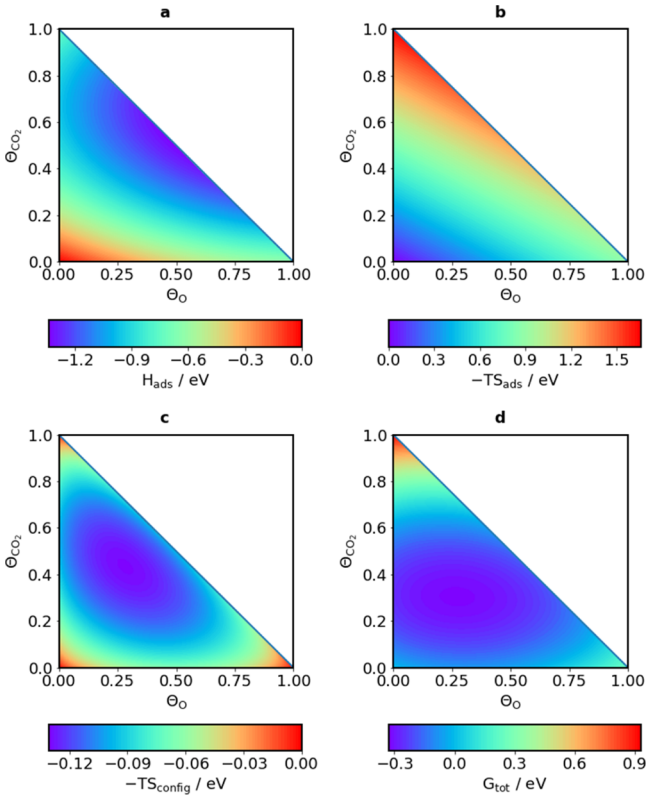

Figure 6. Two-dimensional energy contour maps on the 50% Sr-doped surface showing (a) total adsorption enthalpy, $H_{ads} = \sum_i \Theta_i \Delta H_i^{ads}$, (b) adsorption entropy $-TS_{ads}$, where $S_{ads} = \sum_i \Theta_i \Delta S_i^{ads}$, (c) configurational entropy, $-TS_{config}$, and (d) G_{tot} which is the sum of the three previous terms, with varying Θ_{CO_2} and Θ_O. The plots are shown for T = 1073 K and $p_{O_2} = p_{CO_2}$ = 1 bar.

ranges of 673−1073 K and 0.01−1 bar O_2 and partial pressures of 10^{-10} to 10 bar for the CO_2 and H_2O coadsorbates on the 50% Sr surface. Figure 7 shows the case for O_2/CO_2 coadsorption. Under the considered conditions, Θ_O is hardly influenced by the presence of CO_2 because of the availability of a significant amount of adsorption sites for both species throughout the pressure ranges (Θ_{free}). These results show that coadsorption of O_2 and CO_2 is not in competition with each other. Despite the noncompetitive nature of the CO_2 adsorption, CO_2 adsorbates provide extra oxygen-containing surface species that may be involved in the oxygen exchange reactions. There is a significant contribution from CO_2 to $\Theta_{O_{tot}}$ even at relatively low p_{CO_2}: 10^{-1} bar CO_2 increases $\Theta_{O_{tot}}$ by a factor of 1.7 at 673 K and by a factor of 3.5 at 1073 K relative to the CO_2-free case. CO_2 adsorption becomes negligible for partial pressures lower than 10^{-7} bar at 1073 K.

Figure 8 shows the calculated adsorbate coverages for O_2/H_2O coadsorption in the same temperature and partial pressure range on the 50% Sr-doped LSM surface. The effect of H_2O on O_2 adsorption qualitatively resembles that of CO_2, that is, Θ_O remains almost constant with varying p_{H_2O}. There are major differences as well. Adsorption of H_2O is energetically less favorable compared to that of CO_2 at low coverage but more favorable at high coverage because of weaker adsorbate interactions (Table 1). Consequently, starting from $p_{H_2O} = 10^{-10}$ bar at 673 K, Θ_{H_2O} is initially lower than Θ_{CO_2} under equivalent conditions but increases

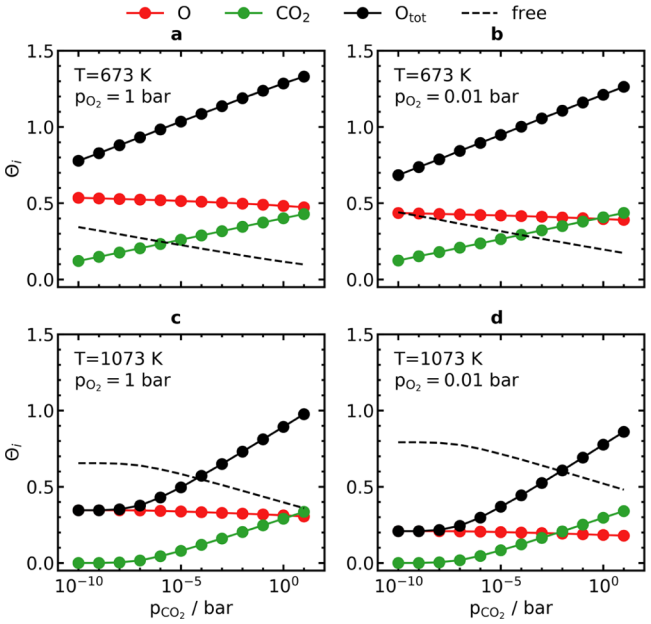

Figure 7. Equilibrium adsorbate concentrations on the 50% Sr-doped LSM surface with varying CO_2 partial pressure at (a) T = 673 K, p_{O_2} = 1 bar; (b) T = 673 K, p_{O_2} = 0.01 bar; (c) T = 1073 K, p_{O_2} = 1 bar; and (d) T = 1073 K, p_{O_2} = 0.01 bar.

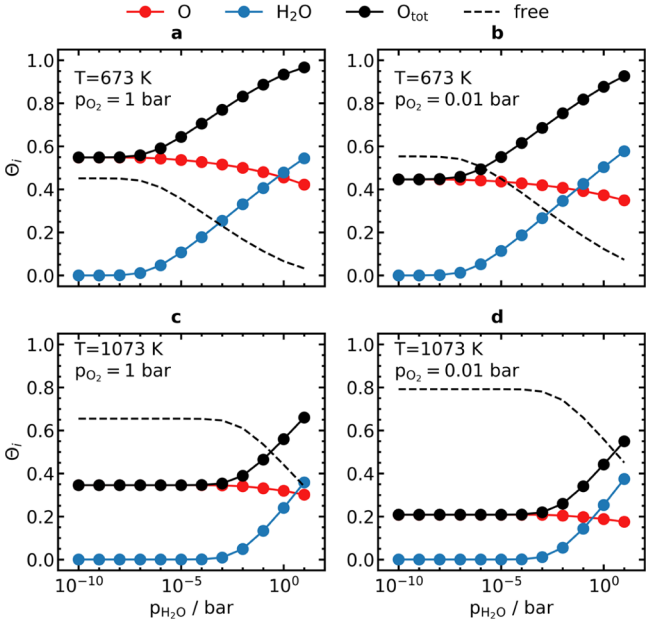

Figure 8. Equilibrium adsorbate concentrations on the 50% Sr-doped LSM surface with varying H_2O partial pressure at (a) T = 673 K, p_{O_2} = 1 bar; (b) T = 673 K, p_{O_2} = 0.01 bar; (c) T = 1073 K, p_{O_2} = 1 bar; and (d) T = 1073 K, p_{O_2} = 0.01 bar.

with a steeper slope with increasing partial pressure. A competitive adsorption regime is entered at around $p_{H_2O} > 10^{-3}$ bar with minor suppression of Θ_O.

Equivalent coverage plots for the 25% and 100 Sr-doped LSM surfaces are provided in Figures S5−S8. The qualitative trends remain similar to those of the 50% Sr-doped surface, in line with the relatively small changes in adsorption energies as shown in Figure 5. There is a moderate decrease in total

https://dx.doi.org/10.1021/acs.chemmater.9b05243
Chem. Mater. 2020, 32, 5483−5492

adsorbate coverages going from the 25% Sr-doped surface to the 100% Sr-doped surface because of the less exothermic adsorption energies with increasing Sr content.

4. DISCUSSION

In this section, we discuss possible connections between surface adsorbate concentrations and the oxygen dissociation rate by comparison with the experimental results from Huang et al.[16] We first assume a simple model for the relationship between the oxygen dissociation rate, R_{diss}, and the total number of active species on the surface, Θ_{act}

$$R_{diss} \propto \Theta_{act} \exp(-E_a/kT) \quad (13)$$

This model assumes that R_{diss} follows an Arrhenius relationship with an activation energy, E_a, that is constant and not affected by coadsorption. The prefactor Θ_{act} represents a nonlinear term because of changes in surface coverage with respect to temperature and partial pressures. In ref 16, the dissociation rate R_{diss} is represented by the measured $[^{18}O^{16}O]$. Huang et al. obtained apparent activation energies of 0.65 eV in 0.5 atm oxygen, 0.89 eV with the addition of 3000 ppm water, and 0.72 eV with the addition of 2500 ppm CO_2.

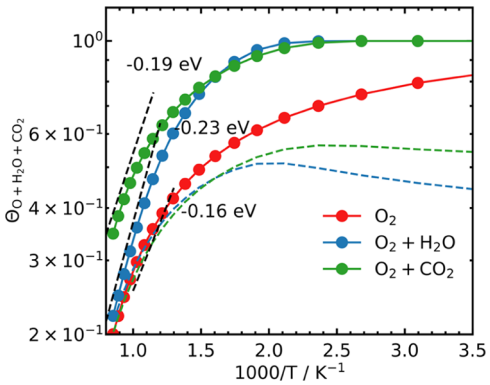

Figure 9. Effect of CO_2 and H_2O on equilibrium $\Theta_{O+H_2O+CO_2}$ predicted in this work in three gas environments varying with temperature (solid lines) on the 50% Sr-doped surface. The three gas environments are all at p_{O_2} = 0.5 atm, with the addition of 3000 ppm H_2O (blue) and 2500 ppm CO_2 (green). For comparison, Θ_O in presence of CO_2/H_2O (dashed lines) shows that there is a negligible effect of coadsorption on Θ_O under these conditions. The contribution of coverage to the apparent activation energy for each case is fitted and shown by the dashed black lines.

Figure 9 shows $\Theta_{O+H_2O+CO_2}$ as a function of inverse temperature under the same gas environments on the 50% Sr-doped surface, assuming that $\Theta_{O+H_2O+CO_2}$ is an appropriate representation of Θ_{act} in eq 13. The Arrhenius relationships are fitted and shown by the dashed black lines. The result shows that changes in $\Theta_{O+H_2O+CO_2}$ with temperature represents a minor contribution to the apparent activation energy: −0.16 eV (for pure O_2) and −0.19 to −0.23 eV (for coadsorption) in the high-temperature regime (973−1123 K). This effect gradually disappears as temperature goes down and the surface becomes saturated.

Now, we discuss whether $\Theta_{O+H_2O+CO_2}$ is a good representation of active species contributing to surface dissociation by referring back to measurements in ref 16. Following eq 13, under the same temperature, the ratio of $[^{16}O^{18}O]$ in the two gas environments should be the same as the ratio of the respective Θ_{act}. In other words, the ratio $\frac{[^{16}O^{18}O]_{O_2}}{[^{16}O^{18}O]_{O_2+H_2O}} = \Theta_{act,O_2}/\Theta_{act,O_2+H_2O}$, where the subscripts O_2 and $O_2 + H_2O$ represent the two gas environments with and without H_2O addition. The same relationship applies to the comparison with and without CO_2. Comparing the three gas atmospheres in Figure 9, Θ_O changes very little with the addition of H_2O or CO_2 because of the noncompetitive nature of the adsorption. Therefore, if the oxygen exchange mechanism remains unchanged in the presence of H_2O and CO_2, these results indicate that Θ_O is not the only source of active surface species.

The two remaining candidates that we consider for Θ_{act} are $\Theta_{O+H_2O+CO_2}$ and $\Theta_{O_{tot}}$. In Figure 10, we show the ratios as in (a)

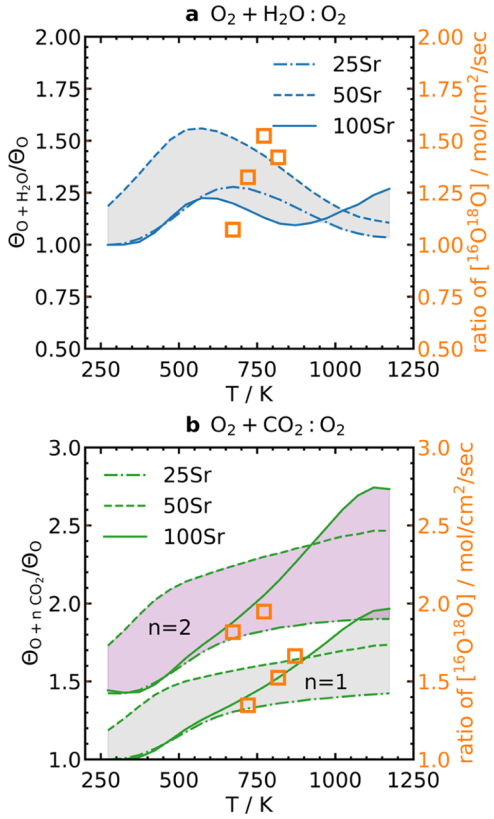

Figure 10. Comparison between predicted $\Theta_{O_{tot}}$, $\Theta_{O+H_2O+CO_2}$, and experimentally measured $^{16}O^{18}O$ steady-state concentration as in ref 16. The lines show the ratio of Θ_{act} in O_2 plus 3000 ppm of water (a) or O_2 plus 2500 ppm of CO_2 (b) vs in pure O_2 on surfaces with 25%−100% Sr contents. The orange squares show the ratio in $[^{16}O^{18}O]$ under the same conditions calculated from data in ref 16.

0.5 atm O_2 plus 3000 ppm H_2O versus pure O_2 and (b) 0.5 atm O_2 plus 2500 ppm CO_2 versus pure O_2 in comparison to the ratio of the measured oxygen exchange rates. The colored bands represent the uncertainty due to the different Sr contents in the surface layer. Looking at Figure 10a, the ratio of Θ_{O+H_2O} goes from 1.2−1.50 at 673 K to 1.05−1.30 at 823 K. A 1.05−1.5 ratio of $[^{16}O^{18}O]$ with and without H_2O was observed experimentally, which is quantitatively close to the increase in $\Theta_{O+H_2O+CO_2}$. In Figure 10b, the ratio between

https://dx.doi.org/10.1021/acs.chemmater.9b05243
Chem. Mater. 2020, 32, 5483−5492

$\Theta_{O+H_2O+CO_2}$ with and without CO_2 ranges from 1.2 to 1.5, which is within the range of the experimental [$^{16}O^{18}O$] ratio. This observation indicates that at least one of the oxygen species in $CO_{3,ad}^{2-}$ can exchange with a neighboring peroxide adsorbate and thereby be active in the homoexchange reaction.

The above quantitative comparison shows that it is reasonable to consider $\Theta_{O+H_2O+CO_2}$ as the prefactor Θ_{act} in eq 13. This will partly eliminate the nonlinear characteristic of the Arrhenius fitting of the oxygen dissociation rate. In Figure 11a,

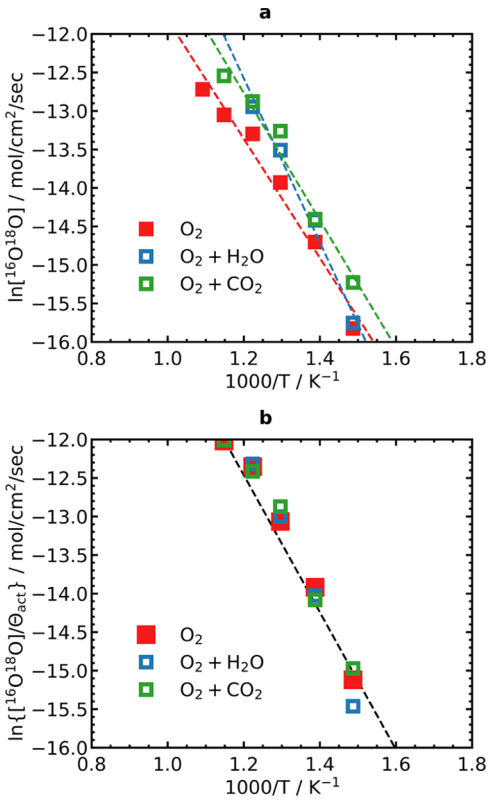

Figure 11. (a) Measured oxygen dissociation rate in 25,000 ppm $^{16}O_2$ and 25,000 ppm $^{18}O_2$ (red) and the effect of 3000 ppm H_2O (blue) and 2500 ppm CO_2 (green) as a function of inverse temperature, adapted with permission from Huang, Y.-L.; Pellegrinelli, C.; Wachsman, E. D. Oxygen Dissociation Kinetics of Concurrent Heterogeneous Reactions on Metal Oxides. *ACS Catal.* **2017**, *7(9)*, 5766−5772.[16] Copyright 2017 ACS. (b) Same data as in (a) normalized by the calculated coverage of active oxygen species on the 50% Sr-doped surface, assuming [$^{16}O^{18}O$] $\propto \Theta_{O+H_2O+CO_2} \exp(-E_a/kT)$. The standard error of the coverage-normalized fit was 0.47 and R^2 = 0.97. For the original data, the apparent activation energies were 0.65 eV (O_2), 0.89 eV (O_2 + H_2O), and 0.72 eV (O_2 + CO_2) with standard errors of 0.69, 0.88, and 0.85, respectively, and R^2 of 0.97, 0.99, and 0.97, respectively.

we reproduce the ln[$^{16}O^{18}O$] versus $1/T$ plot in ref 16 and we compare it to the coverage-normalized ln{[$^{16}O^{18}O$]/$\Theta_{O+H_2O+CO_2}$} versus $1/T$ plot in Figure 11b for the 50%-Sr doped surface. Here, $\Theta_{O+H_2O+CO_2}$ is the calculated value from this work under the experimental thermodynamic conditions. Assuming [$^{16}O^{18}O$] $\propto \Theta_{O+H_2O+CO_2} \exp(-E_a/kT)$, we obtain a uniform activation energy of 0.81 eV for all three atmospheres. The good consistency among all three sets of data after the prefactor normalization indicates that eq 13 is a plausible model for interpreting experimental surface kinetic data and that the increase in Θ_{act} is possibly the predominant contributor to the enhancement of the oxygen dissociation rate in the presence of CO_2 and H_2O.

Figures S10 and S11 presents equivalent renormalized dissociation rates for the 25 and 100% Sr-doped surfaces. Similar to the 50% Sr-doped case, the renormalization allows for a uniform activation energy across gas atmospheres. Activation energies of 0.78 and 0.87 eV were obtained for the 25 and 100% Sr-doped surfaces, respectively.

The present work demonstrates that an increased concentration of oxygen-containing surface species in the presence of small amounts of CO_2 or H_2O ($\Theta_{O+H_2O+CO_2}$) can account for the increase in the oxygen exchange rate according to the homoexchange mechanism. This concentration effect, of course, is not expected to be the only factor that could contribute to the enhanced surface oxygen exchange rate on LSM. It is reasonable to expect that different surface species, such as surface hydroxide and carbonate, can affect the reaction mechanisms in different ways through interactions with the surface and oxygen adsorbates. This could potentially explain some discrepancies between the predicted $\Theta_{O+H_2O+CO_2}$ ratio and experimental oxygen exchange rates. Discrepancies can also be ascribed to several limitations of the model, including the use of a single pristine (0 0 1) surface, lack of interactions between coadsorbates, and computational accuracy (particularly the rather large correction applied to the oxygen adsorption energies, see Section 2.1 and the Supporting Information).

We conclude that the ORR is affected by CO_2/H_2O in the following way when these gases are added in small amounts into O_2 gas. First, our predicted adsorption concentrations have shown that trace amounts of CO_2/H_2O do not hinder surface oxygen adsorption of O_2. Second, the simple Arrhenius model, as in eq 13, leads to quantitative agreement with experimental oxygen dissociation rates. This result indicates that the increase of active oxygen species provided by coadsorbed CO_2 and H_2O can be correlated with promotion of homoexchange. These two points imply that the presence of CO_2/H_2O in the predicted regime will not impede the ORR. In the regime where dissociative adsorption of oxygen is the rate-limiting step, CO_2/H_2O coadsorption promotes the overall ORR by providing extra active oxygen species on the surface. In terms of the role of surface coverage and heteroexchange rate on the electrode performance of SOFCs, H_2O or CO_2 does not take part in the overall fuel cell reactions. Nevertheless, the increased concentration of oxygen species on the cathode in the presence of H_2O and/or CO_2 may promote the kinetics of intermediate reactions that increase performance.

5. CONCLUSIONS

First-principles calculations and thermodynamic models were used to investigate oxygen, water, and carbon dioxide adsorption on the (La, Sr)O-terminated (0 0 1) LSM surface as functions of temperature and partial pressures. The calculated surface coverages showed that adsorption of oxygen was hardly influenced by trace amounts H_2O or CO_2 because of the noncompetitive nature of coadsorption. However, CO_2 and H_2O do contribute significantly to the total number of oxygen-containing surface species, even at low partial pressures. By assuming that these species take part in the oxygen homoexchange reactions, the increase in coverage was

https://dx.doi.org/10.1021/acs.chemmater.9b05243
Chem. Mater. 2020, 32, 5483−5492

compared with experimental values of the oxygen exchange rate on LSM. The results suggest that the change in surface coverage of the oxygen-containing species can account for a major part of the measured increase in the oxygen exchange rate in the presence of CO_2 and H_2O. These results provide a new understanding of the role of surface coverage and coadsorbates on the oxygen exchange rate on LSM surfaces.

■ ASSOCIATED CONTENT

Supporting Information

The Supporting Information is available free of charge at https://pubs.acs.org/doi/10.1021/acs.chemmater.9b05243.

Chemical potential of O_2; adsorption entropies; adsorbate interactions; energy contour maps for H_2O/O_2 coadsorption; coverage plots for 25% Sr-doped and 100% Sr-doped surfaces; and renormalized oxygen dissociation rate on 25% Sr-doped and 100% Sr-doped surfaces (PDF)

■ AUTHOR INFORMATION

Corresponding Authors

Jonathan M. Polfus − *Department of Materials Science and Engineering, Massachusetts Institute of Technology, Cambridge, Massachusetts 02139, United States; Sustainable Energy Technology, SINTEF Industry, NO-0314 Oslo, Norway;* orcid.org/0000-0002-8975-185X; Email: jonathan.polfus@sintef.no

Bilge Yildiz − *Department of Nuclear Science and Engineering and Department of Materials Science and Engineering, Massachusetts Institute of Technology, Cambridge, Massachusetts 02139, United States;* orcid.org/0000-0002-2688-5666; Email: byildiz@mit.edu

Authors

Jing Yang − *Department of Materials Science and Engineering, Massachusetts Institute of Technology, Cambridge, Massachusetts 02139, United States;* orcid.org/0000-0003-1855-0708

Zuoan Li − *Sustainable Energy Technology, SINTEF Industry, NO-0314 Oslo, Norway*

Harry L. Tuller − *Department of Materials Science and Engineering, Massachusetts Institute of Technology, Cambridge, Massachusetts 02139, United States*

Complete contact information is available at: https://pubs.acs.org/10.1021/acs.chemmater.9b05243

Author Contributions

‖J.Y. and J.M.P. equally contributing authors.

Notes

The authors declare no competing financial interest.

■ ACKNOWLEDGMENTS

J.Y. and B.Y. thank the support from the Consortium for Advanced Simulation of Light Water Reactors (CASL), an Energy Innovation Hub for Modeling and Simulation of Nuclear Reactors under U.S. Department of Energy Contract no. DEAC05-00OR22725. J.M.P. and Z.L. acknowledge financial support from the national funding organizations (Research Council of Norway, NWO, MINECO) in the framework of the M-ERA.NET project (grant number 258875) "Designing rules for enhancing SURface KINetics in functional OXides for clean energy technologies" (SURKINOX) and computational resources from Uninett Sigma2 (nn9259k). H.L.T. and B.Y. acknowledge the support for their research from the Department of Energy, Basic Energy Sciences under award number DE-SC0002633 (Chemomechanics of Far-From-Equilibrium Interfaces).

■ REFERENCES

(1) Fleig, J.; Kim, H.-R.; Jamnik, J.; Maier, J. Oxygen Reduction Kinetics of Lanthanum Manganite (LSM) Model Cathodes: Partial Pressure Dependence and Rate-Limiting Steps. *Fuel Cells* **2008**, *8*, 330−337.

(2) Wang, L.; Merkle, R.; Mastrikov, Y. A.; Kotomin, E. A.; Maier, J. Oxygen Exchange Kinetics on Solid Oxide Fuel Cell Cathode Materials—General Trends and Their Mechanistic Interpretation. *J. Mater. Res.* **2012**, *27*, 2000−2008.

(3) Adler, S. B. Factors Governing Oxygen Reduction in Solid Oxide Fuel Cell Cathodes. *Chem. Rev.* **2004**, *104*, 4791−4844.

(4) Kong, J.; Zhang, Y.; Deng, C.; Xu, J. Synthesis and Electrochemical Properties of LSM and LSF Perovskites as Anode Materials for High Temperature Steam Electrolysis. *J. Power Sources* **2009**, *186*, 485−489.

(5) Zhang, G.; Jin, W.; Xu, N. Design and Fabrication of Ceramic Catalytic Membrane Reactors for Green Chemical Engineering Applications. *Engineering* **2018**, *4*, 848−860.

(6) Sun, C.; Hui, R.; Roller, J. Cathode Materials for Solid Oxide Fuel Cells: A Review. *J. Solid State Electrochem.* **2010**, *14*, 1125−1144.

(7) Li, W.; Gong, M.; Liu, X. Characterization of Doped Yttrium Chromites as Electrodes for Solid Oxide Fuel Cell by Impedance Method. *J. Electrochem. Soc.* **2014**, *161*, F551−F560.

(8) Fleig, J. Solid Oxide Fuel Cell Cathodes: Polarization Mechanisms and Modeling of the Electrochemical Performance. *Annu. Rev. Mater. Res.* **2003**, *33*, 361−382.

(9) Gong, M.; Gemmen, R. S.; Mebane, D. S.; Gerdes, K.; Liu, X. Simulation of Surface-Potential Driven ORR Kinetics on SOFC Cathode with Parallel Reaction Pathways. *J. Electrochem. Soc.* **2014**, *161*, F344−F353.

(10) Huang, Y.-L.; Pellegrinelli, C.; Wachsman, E. D. Direct Observation of Oxygen Dissociation on Non-Stoichiometric Metal Oxide Catalysts. *Angew. Chem., Int. Ed.* **2016**, *55*, 15268−15271.

(11) Bertei, A.; Carpanese, M. P.; Clematis, D.; Barbucci, A.; Bazant, M. Z.; Nicolella, C. Understanding the Electrochemical Behaviour of LSM-Based SOFC Cathodes. Part II - Mechanistic Modelling and Physically-Based Interpretation. *Solid State Ionics* **2017**, *303*, 181−190.

(12) Navickas, E.; Huber, T. M.; Chen, Y.; Hetaba, W.; Holzlechner, G.; Rupp, G.; Stöger-Pollach, M.; Friedbacher, G.; Hutter, H.; Yildiz, B.; et al. Fast Oxygen Exchange and Diffusion Kinetics of Grain Boundaries in Sr-Doped LaMnO3 Thin Films. *Phys. Chem. Chem. Phys.* **2015**, *17*, 7659−7669.

(13) Polfus, J. M.; Yildiz, B.; Tuller, H. L. Origin of Fast Oxide Ion Diffusion along Grain Boundaries in Sr-Doped LaMnO3. *Phys. Chem. Chem. Phys.* **2018**, *20*, 19142−19150.

(14) Bouwmeester, H. J. M.; Song, C.; Zhu, J.; Yi, J.; van Sint Annaland, M.; Boukamp, B. A. A Novel Pulse Isotopic Exchange Technique for Rapid Determination of the Oxygen Surface Exchange Rate of Oxide Ion Conductors. *Phys. Chem. Chem. Phys.* **2009**, *11*, 9640−9643.

(15) Li, Z.; Haugsrud, R. Effects of Surface Coatings on the Determination of Dchem and Kchem in $La_2NiO_{4+\delta}$ by Conductivity Relaxation. *Solid State Ionics* **2012**, *206*, 67−71.

(16) Huang, Y.-L.; Pellegrinelli, C.; Wachsman, E. D. Oxygen Dissociation Kinetics of Concurrent Heterogeneous Reactions on Metal Oxides. *ACS Catal.* **2017**, *7*, 5766−5772.

(17) Li, M.; Sun, Z.; Yang, W.; Hong, T.; Zhu, Z.; Zhang, Y.; Wu, X.; Xia, C. Mechanism for the Enhanced Oxygen Reduction Reaction of $La_{0.6}Sr_{0.4}Co_{0.2}Fe_{0.8}O_{3-\delta}$ by Strontium Carbonate. *Phys. Chem. Chem. Phys.* **2017**, *19*, 503−509.

(18) Staykov, A.; Fukumori, S.; Yoshizawa, K.; Sato, K.; Ishihara, T.; Kilner, J. Interaction of SrO-Terminated $SrTiO_3$ Surface with Oxygen, Carbon Dioxide, and Water. *J. Mater. Chem. A* **2018**, *6*, 22662−22672.
(19) Nenning, A.; Navickas, E.; Hutter, H.; Fleig, J. Water-Induced Decoupling of Tracer and Electrochemical Oxygen Exchange Kinetics on Mixed Conducting Electrodes. *J. Phys. Chem. Lett.* **2016**, *7*, 2826−2831.
(20) Téllez Lozano, H.; Druce, J.; Cooper, S. J.; Kilner, J. A. Double Perovskite Cathodes for Proton-Conducting Ceramic Fuel Cells: Are They Triple Mixed Ionic Electronic Conductors? *Sci. Technol. Adv. Mater.* **2017**, *18*, 977−986.
(21) Zhao, Z.; Liu, L.; Zhang, X.; Wu, W.; Tu, B.; Cui, D.; Ou, D.; Cheng, M. High- and Low- Temperature Behaviors of $La_{0.6}Sr_{0.4}Co_{0.2}Fe_{0.8}O_{3-\delta}$ Cathode Operating under CO_2/H_2O-Containing Atmosphere. *Int. J. Hydrogen Energy* **2013**, *38*, 15361−15370.
(22) Lai, S. Y.; Ding, D.; Liu, M.; Liu, M.; Alamgir, F. M. Operando and In Situ X-Ray Spectroscopies of Degradation in $La_{0.6}Sr_{0.4}Co_{0.2}Fe_{0.8}O_{3-\delta}$ Thin Film Cathodes in Fuel Cells. *ChemSusChem* **2014**, *7*, 3078−3087.
(23) Piskunov, S.; Heifets, E.; Jacob, T.; Kotomin, E. A.; Ellis, D. E.; Spohr, E. Electronic Structure and Thermodynamic Stability of $LaMnO_3$ and $La_{1-x}Sr_xMnO_3$ (001) Surfaces: Ab Initio Calculations. *Phys. Rev. B: Condens. Matter Mater. Phys.* **2008**, *78*, 121406.
(24) Druce, J.; Ishihara, T.; Kilner, J. Surface Composition of Perovskite-Type Materials Studied by Low Energy Ion Scattering (LEIS). *Solid State Ionics* **2014**, *262*, 893−896.
(25) Hammami, R.; Batis, H.; Minot, C. Combined Experimental and Theoretical Investigation of the CO_2 Adsorption on $LaMnO_{3+y}$ Perovskite Oxide. *Surf. Sci.* **2009**, *603*, 3057−3067.
(26) Baniecki, J. D.; Ishii, M.; Kurihara, K.; Yamanaka, K.; Yano, T.; Shinozaki, K.; Imada, T.; Nozaki, K.; Kin, N. Photoemission and Quantum Chemical Study of $SrTiO_3$(001) Surfaces and Their Interaction with CO_2. *Phys. Rev. B: Condens. Matter Mater. Phys.* **2008**, *78*, 195415.
(27) Polfus, J. M.; Yildiz, B.; Tuller, H. L.; Bredesen, R. Adsorption of CO_2 and Facile Carbonate Formation on $BaZrO_3$ Surfaces. *J. Phys. Chem. C* **2018**, *122*, 307−314.
(28) Shen, Y.; Wang, W.; Wang, X.; Zhou, Z.; Fei, W. First-Principles Study of CO_2 Adsorption on KNTN (001) Surfaces. *Appl. Surf. Sci.* **2014**, *308*, 269−274.
(29) Kröger, F. A.; Vink, H. J. Relations between the Concentrations of Imperfections in Crystalline Solids. *Solid State Phys.* **1956**, *3*, 307−435.
(30) Kresse, G.; Joubert, D. From Ultrasoft Pseudopotentials to the Projector Augmented-Wave Method. *Phys. Rev. B: Condens. Matter Mater. Phys.* **1999**, *59*, 1758−1775.
(31) Blöchl, P. E. Projector Augmented-Wave Method. *Phys. Rev. B: Condens. Matter Mater. Phys.* **1994**, *50*, 17953−17979.
(32) Perdew, J. P.; Burke, K.; Ernzerhof, M. Generalized Gradient Approximation Made Simple. *Phys. Rev. Lett.* **1996**, *77*, 3865−3868.
(33) Dudarev, S. L.; Botton, G. A.; Savrasov, S. Y.; Humphreys, C. J.; Sutton, A. P. Electron-Energy-Loss Spectra and the Structural Stability of Nickel Oxide: An LSDA+U Study. *Phys. Rev. B: Condens. Matter Mater. Phys.* **1998**, *57*, 1505−1509.
(34) Lee, Y.-L.; Kleis, J.; Rossmeisl, J.; Morgan, D. Ab Initio Energetics of $LaBO_3$ (001) (B=Mn, Fe, Co, and Ni) for Solid Oxide Fuel Cell Cathodes. *Phys. Rev. B: Condens. Matter Mater. Phys.* **2009**, *80*, 1−20.
(35) Jalili, H.; Han, J. W.; Kuru, Y.; Cai, Z.; Yildiz, B. New Insights into the Strain Coupling to Surface Chemistry, Electronic Structure, and Reactivity of $La_{0.7}Sr_{0.3}MnO_3$. *J. Phys. Chem. Lett.* **2011**, *2*, 801−807.
(36) Lee, W.; Han, J. W.; Chen, Y.; Cai, Z.; Yildiz, B. Cation Size Mismatch and Charge Interactions Drive Dopant Segregation at the Surfaces of Manganite Perovskites. *J. Am. Chem. Soc.* **2013**, *135*, 7909−7925.
(37) Wang, Y.; Cheng, H.-P. Oxygen Reduction Activity on Perovskite Oxide Surfaces: A Comparative First-Principles Study of $LaMnO_3$, $LaFeO_3$ and $LaCrO_3$. *J. Phys. Chem. C* **2013**, *117*, 2106−2112.
(38) Pavone, M.; Muñoz-García, A. B.; Ritzmann, A. M.; Carter, E. A. First-Principles Study of Lanthanum Strontium Manganite: Insights into Electronic Structure and Oxygen Vacancy Formation. *J. Phys. Chem. C* **2014**, *118*, 13346−13356.
(39) Choi, Y.; Mebane, D. S.; Lin, M. C.; Liu, M. Oxygen Reduction on $LaMnO_3$-Based Cathode Materials in Solid Oxide Fuel Cells. *Chem. Mater.* **2007**, *19*, 1690−1699.
(40) Atkins, P. W. *Physical Chemistry*, 6th ed.; Oxford University Press: Oxford, 1998.
(41) Chase, M. *NIST-JANAF Thermochemical Tables*, 4th ed.; Journal of Physical and Chemical Reference Data Monograph; American Institute of Physics, 1998.
(42) Wang, L.; Maxisch, T.; Ceder, G. Oxidation Energies of Transition Metal Oxides within the GGA+U Framework. *Phys. Rev. B: Condens. Matter Mater. Phys.* **2006**, *73*, 195107.
(43) Halwidl, D.; Stöger, B.; Mayr-Schmölzer, W.; Pavelec, J.; Fobes, D.; Peng, J.; Mao, Z.; Parkinson, G. S.; Schmid, M.; Mittendorfer, F.; et al. Adsorption of Water at the SrO Surface of Ruthenates. *Nat. Mater.* **2016**, *15*, 450.
(44) Hess, F.; Yildiz, B. Polar or Not Polar? The Interplay between Reconstruction, Sr Enrichment, and Reduction at the $La_{0.75}Sr_{0.25}MnO_3$ (001) Surface. *Phys. Rev. Mater.* **2020**, *4*, 015801.
(45) Kim, D.; Bliem, R.; Hess, F.; Gallet, J.-J.; Yildiz, B. Electrochemical Polarization Dependence of the Elastic and Electrostatic Driving Forces to Aliovalent Dopant Segregation on $LaMnO_3$. *J. Am. Chem. Soc.* **2020**, *142*, 3548−3563.
(46) Shirsat, A. N.; Ali, M.; Kaimal, K. N. G.; Bharadwaj, S. R.; Das, D. Thermochemistry of $La_2O_2CO_3$ Decomposition. *Thermochim. Acta* **2003**, *399*, 167−170.
(47) Robie, R. A.; Hemingway, B. S. Thermodynamic Properties of Minerals and Related Substances at 298.15 K and 1 Bar (10$\hat{5}$ Pascals) Pressure and at Higher Temperatures. *U.S. Geol. Survey Bull.* **1995**, *2131*, 461.
(48) Mei, D. Density Functional Theory Study of Surface Carbonate Formation on BaO(001). *J. Phys. Chem. C* **2010**, *114*, 1867−1874.
(49) Sharma, V.; Mahapatra, M. K.; Krishnan, S.; Thatcher, Z.; Huey, B. D.; Singh, P.; Ramprasad, R. Effects of Moisture on (La, A)MnO_3 (A = Ca, Sr, and Ba) Solid Oxide Fuel Cell Cathodes: A First-Principles and Experimental Study. *J. Mater. Chem. A* **2016**, *4*, 5605−5615.
(50) Staykov, A.; Téllez, H.; Akbay, T.; Druce, J.; Ishihara, T.; Kilner, J. Oxygen Activation and Dissociation on Transition Metal Free Perovskite Surfaces. *Chem. Mater.* **2015**, *27*, 8273−8281.
(51) Evarestov, R. A.; Bandura, A. V.; Alexandrov, V. E. Adsorption of Water on (001) Surface of $SrTiO_3$ and $SrZrO_3$ Cubic Perovskites: Hybrid HF-DFT LCAO Calculations. *Surf. Sci.* **2007**, *601*, 1844−1856.
(52) Bandura, A. V.; Evarestov, R. A.; Kuruch, D. D. Hybrid HF−DFT Modeling of Monolayer Water Adsorption on (001) Surface of Cubic $BaHfO_3$ and $BaZrO_3$ Crystals. *Surf. Sci.* **2010**, *604*, 1591−1597.
(53) Polfus, J. M.; Yang, J.; Yildiz, B. Interplay between H_2O and CO_2 Coadsorption and Space-Charge on Y-Doped $BaZrO_3$ Surfaces. *J. Mater. Chem. A* **2018**, *6*, 24823−24830.
(54) Piskunov, S.; Jacob, T.; Spohr, E. Oxygen Adsorption at $La_{1-x}Sr_xMnO_3$(001) Surfaces: Predictions from First Principles. *Phys. Rev. B: Condens. Matter Mater. Phys.* **2011**, *83*, 73402.
(55) Kotomin, E. A.; Mastrikov, Y. A.; Heifets, E.; Maier, J. Adsorption of Atomic and Molecular Oxygen on the $LaMnO_3$(001) Surface: Ab Initio Supercell Calculations and Thermodynamics. *Phys. Chem. Chem. Phys.* **2008**, *10*, 4644−4649.
(56) Pilania, G.; Ramprasad, R. Adsorption of Atomic Oxygen on Cubic $PbTiO_3$ and $LaMnO_3$ (001) Surfaces: A Density Functional Theory Study. *Surf. Sci.* **2010**, *604*, 1889−1893.

https://dx.doi.org/10.1021/acs.chemmater.9b05243
Chem. Mater. 2020, 32, 5483−5492